Flutter derivatives from free decay tests of a rectangular B/D=10 section estimated by optimized system identification methods

Michael Styrk Andersen[a,*], Ole Øiseth[b], Jens Johansson[c], Anders Brandt[d]

[a] *Ph.D. Student, M.Sc., University of Southern Denmark, Department of Civil Engineering, Campusvej 55, DK-5230, Odense M*
[b] *Associate Professor, Ph.D., Norwegian University of Science and Technology, Department of Structural Engineering, Richard Birkelands vei 1A, NO-7491 Trondheim*
[c] *M.Sc., Ph.D., Svend Ole Hansen Aps, Sankt Jørgens all 5C, DK-1615 Copenhagen V*
[d] *Associate Professor, Lic.Techn., University of Southern Denmark, Department of Mechanical Engineering, Campusvej 55, DK-5230, Odense M*

Abstract

The present paper suggests a hybrid system identification method to estimate the flutter derivatives from coupled free vibration tests. An optimized covariance-based method is used as the initial guess in the modified unifying least squares method. This combination optimizes the accuracy described by the coefficients of determinations between measured and synthesized signals. Flutter derivatives are identified at high wind speeds, close to and even above the critical flutter wind speed. Results for a sharp-edged rectangular section with a width-to-depth ratio $B/D = 10$ are presented for two different torsional-to-vertical frequency ratios. In one case the torsional frequency are lower than the vertical, due to a high mass moment of inertia, which makes it possible to estimate the flutter derivatives at very high reduced wind speeds. This reveals that the torsional aerodynamic damping derivative A_2^* reaches a positive maximum followed by a continuous decreasing tendency and eventually negative A_2^* values are identified. This implies that torsional flutter for the $B/D = 10$ section can be avoided if the structural damping is designed to balance the negative torsional aerodynamic damping expressed by the positive peak value for A_2^*.

Keywords: Torsional Flutter; Coupled Flutter; Flutter Derivatives; Free Vibration; System identification; Aeroelasticity

*Corresponding author, mian@iti.sdu.dk. University of Southern Denmark, Department of Civil Engineering, Campusvej 55, DK-5230, Odense M

1. Introduction

The objective of the present work is to describe the self-excited forces, also known as the motion induced or unsteady aerodynamic forces, of a sharp-edged rectangular section with a width-to-depth ratio, $B/D = 10$. The self-excited forces are usually expressed by a parametric representation of the flutter derivatives (FD's), A_i^* and H_i^* $(i = 1, 2, 3, 4)$. These are defined as functions of the reduced wind speed, $U/(\omega B)$, where B is the bridge deck width, U is the mean wind speed and $\omega = 2\pi f$ is the circular frequency of motion. It is the aim of the present work to estimate, evaluate and enhance the accuracy and precision of the flutter derivatives estimated from coupled free vibration tests.

The $B/D = 10$ section is known to be prone to single degree of freedom torsional flutter [20] because of positive A_2^* values, which indicate negative aerodynamic damping for the torsional degree of freedom. However, negative A_2^* values have been estimated for the same section by free vibration tests with low amplitudes [21] and recent results for coupled free vibration tests with larger amplitudes [2] showed that both torsional and coupled flutter were avoided when the torsional natural frequency in still air, $\omega_\alpha = 2\pi f_\alpha$, was lower than the vertical, $\omega_h = 2\pi f_h$. The latter indicates that A_2^* is close to zero or even negative at higher reduced wind speeds.

The FD's estimated by system identification methods of wind tunnel tests, which can be either forced motion or free vibration tests, express the damping and stiffness in the fluid-structure system. Since the motion of a real bridge is complex and may have a broadbanded response spectrum, both forced motion tests and coupled free decay tests relies on the principle of superposition of aeroelastic forces. If the principle of superposition holds, the flutter derivatives should be independent of the motion. This implies that the FD's estimated by forced motion and free decay tests should be identical.

It is often assumed that the FD's depends mainly on the geometry of the bridge cross section, see e.g. [11, 25, 33]. Amplitude of motion and wind turbulence can however possibly influence the FD's [23, 29]. Even small discrepancies in the estimated FD's may cause large differences in the calculated critical flutter wind speed [18, 26]. The accuracy of the experimental models and the flutter derivatives estimated by system identification methods are therefore of crucial importance.

1.1. Free vibration system identification methods

Scanlan and Tomko estimated the flutter derivatives, by free vibration tests in [28]. First, two single degree of freedom (SDOF) free decays were used to estimate the 'direct' derivatives (H_1^*, A_2^*, A_3^*) and then a coupled two degree of freedom (2DOF) free decay was used to estimate A_1^*, H_2^* and H_3^*. Their pioneering work relied on the principle of superposition of the aeroelastic forces and that $H_4^* = A_4^* = 0$. Ibrahim and Mikulcik [12] introduced a MDOF time-domain method known as the Ibrahim time-domain method (ITD) where a multi degree of freedom state space representation of a structure was estimated by using only a single free decay test where the response of several degrees

of freedom were measured simultaneously. Sarkar and Scanlan [27] developed a modified Ibrahim time-domain method (MITD) where the original ITD was used as the starting point in an iteration procedure aiming to improve the damping estimate given by ITD. This method allowed the simultaneously estimation of 8 FD's, H_i^* and A_i^* (i=1-4), by a single free decay test.

Poulsen et al. [25] estimated the flutter derivatives for the Great Belt Bridge by minimizing the residual sum of squares between the measured coupled free vibrations and the response predicted by the estimated model parameters based on Newton-Raphson iterations. Different torsional-to-vertical frequency ratios ranging from $\gamma_\omega = 1.4$ to $\gamma_\omega = 3.4$ were tested for this section and no frequency ratio dependency was observed. Each test was repeated 10 times in order to minimize the statistical uncertainty. Gu et al. minimized the residual sum of squares in the unifying least squares (ULS) method where an unified error function for the vertical and torsional degree of freedom was introduced. The initial estimate was given by the MITD [27] method [10]. The ULS method was used to show that the still air mechanical properties had *almost* no effect on the estimated FD's in a parametric study of the streamlined Jiangyn Bridge in [11].

Li et al. introduced weighting factors to the ULS method aiming to scale the vertical and torsional signals to have the same root mean square value [17]. The iterative procedure used in the ULS method was enhanced in the modified unifying least squares (MULS) method by Bartoli et al. [3]. A variation of the MULS method is the improved stochastic search algorithm by Xu et al. [34] which uses random variation of the modal parameter in the iterative scheme.

Juang and Pappa [16] developed the Eigensystem Realization Algorithm (ERA), where the measured time-domain free responses are organized in a general block-Hankel matrix and a time-shifted block-Hankel matrix. The singular values and singular vectors of the general block-Hankel matrix are used to estimate the model parameters. Since the theoretical auto-covariance functions of the response of a white noise excited linear structure are identical to a theoretical free decay of the same structure, the covariance functions of random response measurements can be used within the classic ERA algorithm. This is utilized in the covariance block-Hankel matrix (CBHM) method [4, 13, 14] and in the covariance driven stochastic subspace identification (COV-SSI) method [9].

It was shown by Jakobsen [13] that the theoretical auto covariance function of a SDOF free decay is identical to the free decay itself. Thus, it is also possible to use the covariance driven methods to estimate the FD's from coupled free decay tests, which will be used as the initial estimate for the MULS method in the present work. However, it is well known that the covariance driven methods are sensitive to the number of points (i.e. discrete time lag values) used from the estimated covariance functions [4, 9]. Therefore, in the present work, the model parameters are estimated using several different number of time lags, where the accuracy is evaluated for each.

In addition to the wind tunnel techniques discussed in the present paper, it is also possible to use computational fluid dynamics to estimate bridge deck flutter derivatives. Numerical simulation of the free vibration method are conducted

in [32].

1.2. Torsional Flutter

The rectangular section with a width-to-depth ratio, $B/D = 10$, is known to have hybrid flutter properties [21] because both coupled flutter and torsional flutter can be observed. In [21] it was shown by free vibration tests, that A_2^* was negative for small angular vibration amplitudes and positive for larger. These results have not received much attention in the literature [5, 6, 20, 22, 26] where several references instead are given to later works [20, 22]. In [20, 22], the estimated FD's for the $B/D = 10$ section are obtained by SDOF harmonic forced motion tests and simultaneous pressure measurements. Based hereon it is suggested, generally, that torsional flutter instability occurs for rectangular sharp-edged sections with $B/D \leq 10$ while coupled flutter occurs if $B/D \geq 12.5$. This is not in agreement with [21] and was not confirmed for the $B/D = 10$ section recently published in [2]. Because of the contradictory results for A_2^* in the past, this issue needs to be investigated in more detail.

1.3. Present paper

The present paper is organized as follows. Wind tunnel free vibration tests and procedures are described in Section 2. In Section 3, the equations of motion for free decay tests are defined. A validation method, based on the R^2 coefficients of determination, is introduced in Section 4 in order to evaluate the estimated model parameters. The most accurate modal parameters estimated by an iterative variation of CBHM method [4, 13, 14] where the number of time lags is optimized are used as the initial estimate for the MULS method [3]. The influence of measurement time, number of time lags and accuracy of the initial estimate on the final accuracy of the MULS estimates are described in Section 4.3. It is shown that the flutter derivatives can be estimated after the onset of flutter by the present combination of the CBHM and MULS method. In Section 5, the estimated flutter derivatives are presented and compared with results known from the literature. Furthermore, the influence of static rotations and the pitching motion amplitude on the flutter derivatives are investigated. The estimated FD's presented in Section 5 are used in an iterative mode by mode flutter analysis presented in Section 6.

2. Wind tunnel tests

The spring suspended section model shown in Figure 1 was subjected to free decay tests in the wind tunnel at Svend Ole Hansen Aps in Copenhagen, Denmark. Initial vertical and torsional conditions were obtained by using an electromagnetic release system. The length, width and depth of the section were $L = 1.7$ m, $B = 0.24$m and $D = 0.024$ m respectively. Drag wires were used to restrain the lateral degree of freedom during the tests. The static angle of rotation of the section was set as close to zero as possible by using a digital inclinometer on the section model before the free decay tests were conducted.

At each wind speed, five free decay tests were conducted and the response was measured in 120 seconds with a sampling rate of $f_s = 500$ Hz. The initial torsional displacement in the free decays was $\alpha_0 \approx 4.8$°deg while the vertical initial conditions were $h_0 \approx -43$ and -51 mm for series 1A and 1G respectively. More details about the tests are available in [2]. The displacements of the section was obtained from a linear relation between the measured forces in loadcells which the springs were connected to, previously described in [2].

The data of the individual test series of importance for the present work are given in Table 1 where the equivalent mass and mass moment of inertia per unit length are denoted by m_e and I_e. These were estimated from the natural frequencies in still air and the stiffness of the rig, i.e. added mass effects are included. The torsional-to-vertical frequency ratio, $\gamma_\omega = \omega_\alpha/\omega_h = f_\alpha/f_h$ were adjusted by the mass moment of inertia, i.e. the torsional stiffness remained unchanged between the two test series. The highest wind speed for which the system was stable is denoted U_1 and the lowest wind speed for which the system was observed to be unstable is denoted U_2. The critical flutter wind speed is located between U_1 and U_2. At the highest reached tunnel wind speed for series 1A the system remained stable.

Table 1: Mechanical properties of test series in still air

Test series	γ_ω -	f_h Hz	m_e kg/m	I_e kgm^2/m	U_1 m/s	U_2 m/s
1A	0.71	1.17	11.23	0.50	11.13	
1G	1.19	1.17	11.23	0.18	5.10	6.12

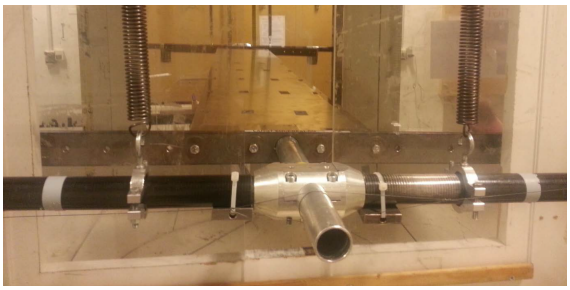

Figure 1: The rectangular $B/D = 10$ section in the wind tunnel. From [15].

.

Examples of the measured free decays at the highest reached wind speeds for which the systems were stable and their corresponding transient spectra are shown in Figure 2. The two spectral peaks for the vertical response indicates the strong degree of aerodynamic coupling between the two modes at high wind

speeds. It can also be seen in the initial part of the time domain data, that the response of the vertical DOF, h, is governed by both modes.

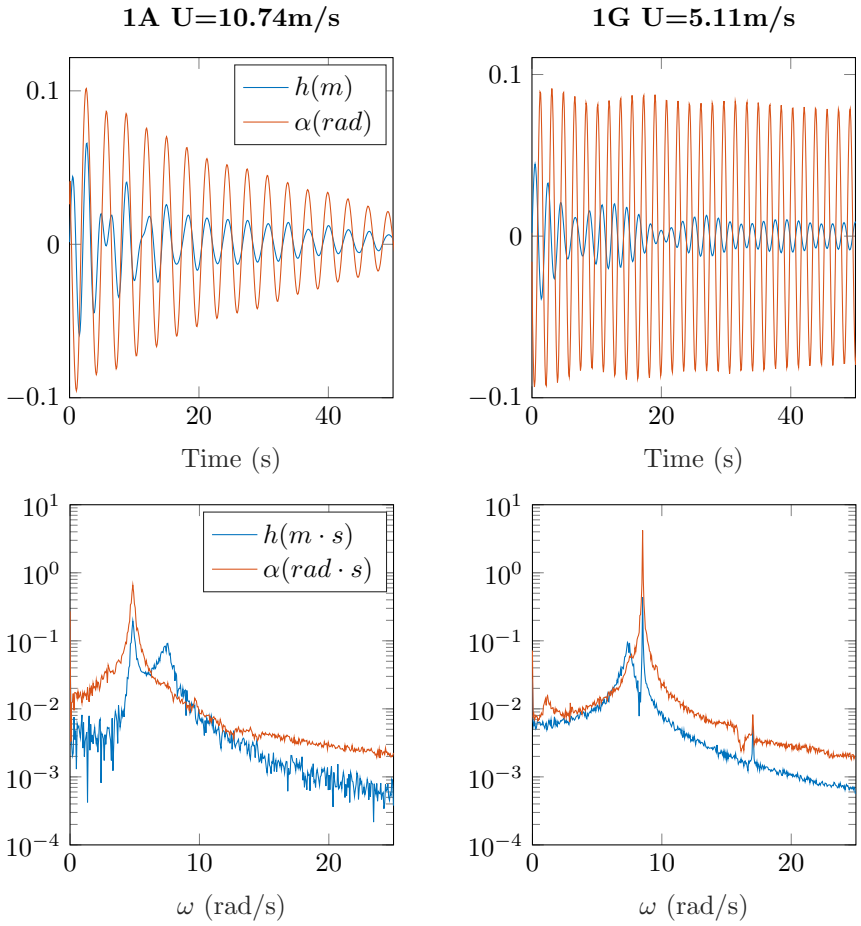

Figure 2: Free decays as measured (above) and the corresponding transient spectra (below)

3. Equations of motion

The equation of motion for the section model subjected to self-excited forces can be expressed in matrix form,

$$\mathbf{M}\ddot{\mathbf{y}} + \mathbf{C^0}\dot{\mathbf{y}} + \mathbf{K^0}\mathbf{y} = \mathbf{C^{ae}}(U,\omega)\dot{\mathbf{y}} + \mathbf{K^{ae}}(U,\omega)\mathbf{y} \tag{1}$$

where the mechanical still air properties of the section are given on the left hand side and the self-excited forces are given on the right-hand side. The

sign convention of the displacements, $\mathbf{y} = \begin{bmatrix} h, & \alpha \end{bmatrix}^\intercal$ are illustrated in Figure 3. The mechanical still air properties of the section are given by the equivalent mass, damping and stiffness matrices per unit length, $\mathbf{M}$, $\mathbf{C^0}$ and $\mathbf{K^0}$ respectively. The mass matrix is a diagonal matrix where the diagonal elements are $\text{diag}(\mathbf{M}) = \begin{bmatrix} m_{eq}, & I_{eq} \end{bmatrix}$. The damping and stiffness matrices are estimated by system identification of the measured free decays. The equivalent aerodynamic damping and stiffness matrices are defined by,

$$\begin{aligned} \mathbf{C^{ae}}(U,\omega) &= \frac{1}{2}\rho U^2 B^2 K \begin{bmatrix} H_1^*/(UB) & H_2^*/U \\ A_1^*/U & BA_2^*/U \end{bmatrix}, \\ \mathbf{K^{ae}}(U,\omega) &= \frac{1}{2}\rho U^2 B K^2 \begin{bmatrix} H_4^*/B & H_3^* \\ A_4^* & B^2 A_3^* \end{bmatrix}, \end{aligned} \tag{2}$$

where the non-dimensional reduced frequency, K is given by $K(U,\omega) = \omega B/U$. It has recently been discussed which frequency to use for the reduced frequency, K, and the estimated FD's in [5, 33]. In the present work, the frequencies, ω_h and ω_α are uniquely identified for each free decay and thus ω_h is used for H_1^*, H_4^*, A_1^*, A_4^* and ω_α is used for A_2^*, A_3^*, H_2^*, H_3^*.

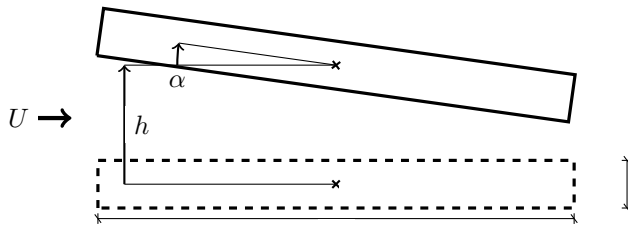

Figure 3: 2DOF Section Model

If the displacement and velocity dependent aerodynamic matrices are moved to the left hand side, the equation of motion is reduced to

$$\mathbf{M}\ddot{\mathbf{y}} + \mathbf{C^e}\dot{\mathbf{y}} + \mathbf{K^e}\mathbf{y} = \mathbf{0} \tag{3}$$

where the effective damping and stiffness matrices are defined by $\mathbf{C^e} = \mathbf{C^0} - \mathbf{C^{ae}}$ and $\mathbf{K^e} = \mathbf{K^0} - \mathbf{K^{ae}}$ respectively. A state space representation of the equation of motion is given by

$$\dot{\mathbf{x}} = \mathbf{A^e}\mathbf{x}, \qquad \mathbf{x} = \begin{bmatrix} \mathbf{y} & \dot{\mathbf{y}} \end{bmatrix} \tag{4}$$

where the effective state space system matrix, $\mathbf{A^e}$, can be estimated by system identification of the coupled free vibration tests of the section model in the wind tunnel.

$$\begin{aligned} \mathbf{A^e} &= \begin{bmatrix} \mathbf{0} & \mathbf{I} \\ -\mathbf{M}^{-1}\mathbf{K^e} & -\mathbf{M}^{-1}\mathbf{C^e} \end{bmatrix}, \\ \mathbf{0} &= \begin{bmatrix} 0 & 0 \\ 0 & 0 \end{bmatrix}, \qquad \mathbf{I} = \begin{bmatrix} 1 & 0 \\ 0 & 1 \end{bmatrix} \end{aligned} \tag{5}$$

It can be seen that the effective stiffness and damping matrix are given by

$$\mathbf{K^e} = -\mathbf{M}\mathbf{A}^{\mathbf{e}}_{(\mathbf{2},\mathbf{1})}, \qquad \mathbf{C^e} = -\mathbf{M}\mathbf{A}^{\mathbf{e}}_{(\mathbf{2},\mathbf{2})} \tag{6}$$

Assuming that the aerodynamic damping and stiffness is zero in still air, the aerodynamic matrices are given by the differences between the effective matrices in still air and in wind. This implies that the flutter derivatives can be expressed as functions of the estimated aerodynamic damping and stiffness matrix coefficients, also dependent on wind speed and frequency.

$$\begin{aligned}
H_1^* &= \frac{2C_{1,1}^{ae}}{\rho B^2 \omega_h} & H_2^* &= \frac{2C_{1,2}^{ae}}{\rho B^3 \omega_\alpha} \\
H_3^* &= \frac{2K_{1,2}^{ae}}{\rho B^3 \omega_\alpha^2} & H_4^* &= \frac{2K_{1,1}^{ae}}{\rho B^2 \omega_h^2} \\
A_1^* &= \frac{2C_{2,1}^{ae}}{\rho B^3 \omega_h} & A_2^* &= \frac{2C_{2,2}^{ae}}{\rho B^4 \omega_\alpha} \\
A_3^* &= \frac{2K_{2,2}^{ae}}{\rho B^4 \omega_\alpha^2} & A_4^* &= \frac{2K_{2,1}^{ae}}{\rho B^3 \omega_h^2}
\end{aligned} \tag{7}$$

4. System identification methods

The present authors agree with [3] that the most reliable way to investigate the accuracy of the estimated model parameters is to compare the measured signal, $\mathbf{y}$, with a numerical simulation, $\hat{\mathbf{y}}$, based on the estimated mechanical and aerodynamic model parameters. However, the comparison should preferably be based on a quantitative method rather than pure visual inspection of the signals as was used in [3].

Several authors, including [3, 10, 17, 25], have used least squares regression to minimize the objective function, J, which is the residual sum of squares between measured decays and numerical simulations obtained using the estimated model parameters.

$$J = \sum_{i=1}^{N} (y_i - \hat{y}_i)^2 \tag{8}$$

Instead of using J which is sensitive to the units used for the vertical and torsional signals and the length of the signal, we propose using the R^2 coefficient of determination

$$R^2 = 1 - \frac{J}{S} \tag{9}$$

where S is the total sum of squares,

$$S = \sum_{i=1}^{N} (y_i - \bar{y})^2 \tag{10}$$

The mean value of the measured signal $\mathbf{y}$ is denoted $\bar{y}$. The accuracy of the estimated model parameters for the two degrees of freedom system is expressed by the joint coefficient of determination,

$$R_h^2 R_\alpha^2 = \left[1 - \frac{\sum_{i=1}^{N}(h_i - \hat{h_i})^2}{\sum_{i=1}^{N}[h_i - \bar{h}]^2}\right] \times \left[1 - \frac{\sum_{i=1}^{N}(\alpha_i - \hat{\alpha_i})^2}{\sum_{i=1}^{N}[\alpha_i - \bar{\alpha}]^2}\right] \tag{11}$$

where the i'th sample of the measured vertical and torsional response is denoted h_i and α_i while the numerical simulated samples are denoted $\hat{h}_i$ and $\hat{\alpha}_i$. The number of samples used here is $N = 5000$, starting at the first zero crossing of the measured vertical signal, h. The numerical simulation of the coupled vertical and torsional free decay is obtained by the sum of two modal contributions expressed by

$$\begin{aligned} \hat{h}(t) &= q_{0h}\phi_h^h e^{\lambda_h t} + q_{0h}\phi_h^{h*} e^{\lambda_h^* t} + q_{0\alpha}\phi_\alpha^h e^{\lambda_\alpha t} + q_{0\alpha}\phi_\alpha^{h*} e^{\lambda_\alpha^* t} \\ \hat{\alpha}(t) &= q_{0h}\phi_h^\alpha e^{\lambda_h t} + q_{0h}\phi_h^{\alpha*} e^{\lambda_h^* t} + q_{0\alpha}\phi_\alpha^\alpha e^{\lambda_\alpha t} + q_{0\alpha}\phi_\alpha^{\alpha*} e^{\lambda_\alpha^* t} \end{aligned} \tag{12}$$

where * is the complex conjugated operator. The model parameters, i.e. the complex eigenvalues and mode shapes estimated by system identification, are given by

$$\begin{aligned} \phi_j &= \left[\phi_j^h, \phi_j^\alpha\right]^\intercal \quad j \in \{h, \alpha\} \\ \lambda_j &= -\zeta_j \omega_{0j} + \omega_{0j}\sqrt{1-\zeta_j^2}\, i \end{aligned} \tag{13}$$

where ω_{0j} is the undamped frequency of mode j and q_{0j} are constants depending on the initial conditions of the measured free decay.

4.1. Iterative covariance driven identification method

The complex eigenvalues and mode shapes are first estimated by the CBHM method [14], using $m = 25$ discrete time lags of the covariance functions. The joint coefficient of determination, $R_h^2 R_\alpha^2$, is calculated and saved. Another time lag is added to the analysis for each iteration until $m = 75$. For each free decay, the procedure is as follows.

The measured torsional and vertical signals are organized in the output matrix, $\mathbf{y} = \begin{bmatrix}\mathbf{h}, & \alpha\end{bmatrix}$. The initial part of the measured response before the first vertical zero crossing is discarded and the remaining part of $\mathbf{y}$ is detrended. An unbiased covariance estimator is used to calculate the covariance function matrix, $\mathbf{R_{yy}}(\tau)$, where τ is the discrete time lag. The first five samples of τ are discarded and the next m lags of the covariance functions are organized in the generalized block-Hankel matrix,

$$\mathbf{H_1} = \begin{bmatrix} [\mathbf{R_{yy}}(6)] & [\mathbf{R_{yy}}(7)] & \cdots & [\mathbf{R_{yy}}(6+m)] \\ [\mathbf{R_{yy}}(7)] & [\mathbf{R_{yy}}(8)] & & [\mathbf{R_{yy}}(7+m)] \\ \vdots & & & \\ [\mathbf{R_{yy}}(6+m)] & [\mathbf{R_{yy}}(7+m)] & \cdots & [\mathbf{R_{yy}}(6+2m)] \end{bmatrix} \tag{14}$$

which is subjected to singular value decomposition,

$$\mathbf{H} = \mathbf{U}\mathbf{\Sigma}\mathbf{V}^{*} \tag{15}$$

where * is the Hermitian transpose operator. The measured free decays represent a 2DOF model which implies that the state space system matrix has the order $n = 4$. The state space system matrix in discrete time, $\mathbf{A_d}$, and in continous time, $\mathbf{A_c}$ and their eigenvalues are realized similar to the ERA method [16] where the discrete state space system matrix is given by

$$\mathbf{A_d} = \left[\mathbf{\Sigma}_{n\times n}\right]^{-1/2} \left[\mathbf{U}_{2m\times n}\right]^{\intercal} \mathbf{H_2} \left[\mathbf{\Sigma}_{n\times n}\right]^{-1/2} \qquad \in \mathbb{R}^{n\times n} \tag{16}$$

where $\mathbf{\Sigma}_{n\times n}$ is a diagonal matrix with the first n singular values, $\mathbf{U}_{2m\times n}$ are the first n columns of the left-singular vector matrix, $\mathbf{U}$ and $\mathbf{H_2}$, is the time-shifted block-Hankel matrix.

$$\mathbf{H_2} = \begin{bmatrix} [\mathbf{R_{yy}}(7)] & [\mathbf{R_{yy}}(8)] & \cdots & [\mathbf{R_{yy}}(7+m)] \\ [\mathbf{R_{yy}}(8)] & [\mathbf{R_{yy}}(9)] & \cdots & [\mathbf{R_{yy}}(8+m)] \\ \vdots & & & \\ [\mathbf{R_{yy}}(7+m)] & [\mathbf{R_{yy}}(8+m)] & \cdots & [\mathbf{R_{yy}}(7+2m)] \end{bmatrix} \tag{17}$$

Eigenvalue decomposition of $\mathbf{A_d}$ yields,

$$\mathbf{A_d}\phi = \lambda_{\mathbf{d}}\phi, \qquad |(\mathbf{A_d} - \lambda_{\mathbf{d}}\mathbf{I}| = 0, \qquad \{\phi, \lambda_{\mathbf{d}}\} \in \mathbb{C}^{n\times n} \tag{18}$$

Transformation of the discrete eigenvalues and state space system matrix to continuous time is conducted as described in [16]. The continuous state space system matrix is transformed to the effective equivalent coordinates used in Equation (5), which is described in [13]. Finally, the flutter derivatives is obtained by Equation (7).

4.2. Modified unifying least squares method

The complex eigenvalues estimated by the CBHM method having the highest $R_h^2 R_\alpha^2$ value are used to define the initial estimate in the present implementation of the MULS method. The iterative procedures in the ULS/MULS methods are described in [3, 10, 17]. In the present implementation, the weighted error functions described by [17] are used together with the enhanced iteration procedure given in [3]. Time histories of 10 seconds starting at the first zero crossing for the vertical signal are used in the iterative scheme. The iterations continue until the residual sum of squares, J, is reduced by less than $\partial J < 10^{-12}$ between two iteration steps and the change in the estimated eigenvalues are less than $\partial\lambda = 10^{-10}$. If this criterion is not reached within the first 150 iteration steps, the iterations are stopped. Convergence is generally reached if there is a good initial estimate of the complex eigenvalues. Finally, the effective damping and system matrices are obtained from the estimated complex eigenvalues and mode shapes as described in [3, 10, 17].

4.3. Robustness and Sensitivity

The performance and the sensitivity of the system identification methods described above are shown in Figure 6. It is seen that the number of time lags used is important for the covariance driven method. The best estimates by the CBHM method are generally slightly enhanced by the MULS method at the cost of increased computational time which is shown in Table 2 for the tests conducted in the pre-critical flutter regime. Using the combined iterative CBHM/MULS method, a joint coefficient of determination, $R_h^2 R_\alpha^2 > 0.99$, were obtained for 44 out of 45 free decay tests in series 1A and for 27 out of 28 free decay tests below the critical wind speed in series 1G.

Table 2: Average computational time and accuracy

		Time (s)		$R_h^2 R_\alpha^2 (\%)$	
Series	Free decay tests	CBHM	MULS	CBHM	MULS
1A	45	7.21	17.27	99.40	99.69
1G	28	7.28	17.42	99.09	99.70
All	73	7.24	17.32	99.29	99.70

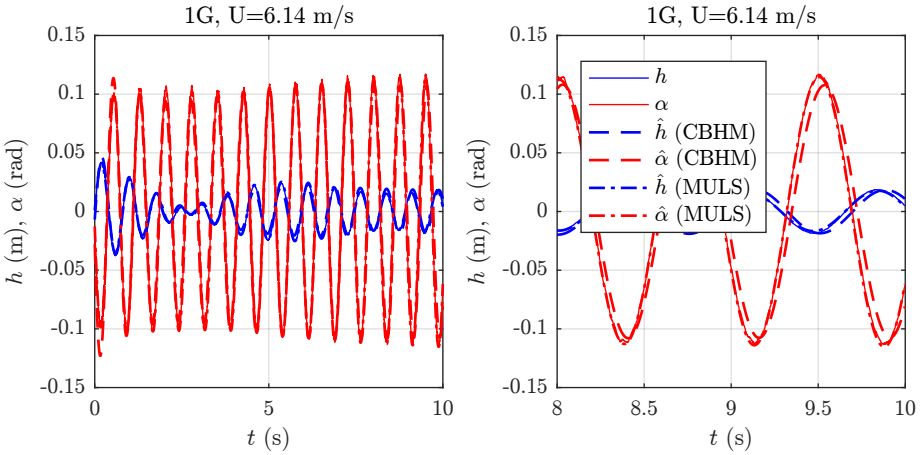

Figure 4: Illustration of the measured and simulated response during flutter. The right plot zooms in on the two last seconds of the time histories

4.3.1. Measurement time

It may seem superfluous to measure 120 seconds when only 10 seconds are used by the MULS method. But the variance of covariance function estimates, and hence the accuracy of initial estimates used in the MULS method depend on the measurement time. The signal-to-noise ratio is highest in the first part of the free decay, which is the reason why it is the first 10 seconds that should

be used to estimate the FD's. If the covariance functions are estimated by using the first 20 instead of all 120 seconds, the average $R_h^2 R_\alpha^2$ values for all tests given in Table 2 are reduced to 98.9% and 99.5% for the CBHM and MULS methods, respectively. It is therefore not suggested to reduce the measurement time even though the final MULS estimate [3] is obtained from the first 10 seconds only. This point does, however, only applies to linear systems. During flutter, nonlinear aerodynamic effects due to the pitching motion amplitude should be avoided by using only the initial part of the time history which is discussed in Section 4.6.

4.4. Effective damping and stiffness matrices in still air

The still air effective damping and stiffness matrices estimated by the MULS method are shown in Table 3. It can be seen that the off diagonals in the stiffness matrix are small compared to the diagonals, which indicates low mechanical coupling.

Table 3: Damping and stiffness matrices estimated in still air with the MULS method [3].

Series	Accuracy $R_h^2 R_\alpha^2$	Damping $\mathbf{C^0}$	Stiffness $\mathbf{K^0}$
1A	99.72	$\begin{bmatrix} 0.405 & 0.036 \\ 0.013 & 0.025 \end{bmatrix}$	$\begin{bmatrix} 610.28 & 0.28 \\ 0.38 & 13.63 \end{bmatrix}$
1G	99.6	$\begin{bmatrix} 0.52 & 0.017 \\ 0.009 & 0.017 \end{bmatrix}$	$\begin{bmatrix} 610.38 & 0.72 \\ 0.35 & 13.62 \end{bmatrix}$

4.5. Validation

A good fit to the measured response is obtained from the estimated model parameters as illustrated in Figure 5. The transient spectra in Figure 5b show that two distinct modes are present at the highest wind speeds reached. However, due to aerodynamic coupling, most of the energy in the vertical DOF, h, is obtained from the mode which eigenvalues are given by λ_α because the participation of the vertical degree of freedom, h, in the torsional dominated mode shape, ϕ_α, increases at higher wind speeds.

4.6. System identification after the onset of flutter

The $R_h^2 R_\alpha^2$ values in the post critical flutter regime for series 1G were generally lower than in the pre-critical regime. Totally, 5 tests were conducted above the critical flutter wind speed. The CBHM method obtained a maximum joint coefficient of determination of $R_h^2 R_\alpha^2 = 0.93$. The maximum number of iterations used in the MULS method was therefore increased to 500 which resulted in two out of five tests achieving $R_h^2 R_\alpha^2 > 0.99$ in the post-critical flutter regime. An example of the measured and simulated response for the described CBHM and MULS estimation after the onset of flutter are shown in Figure 4.

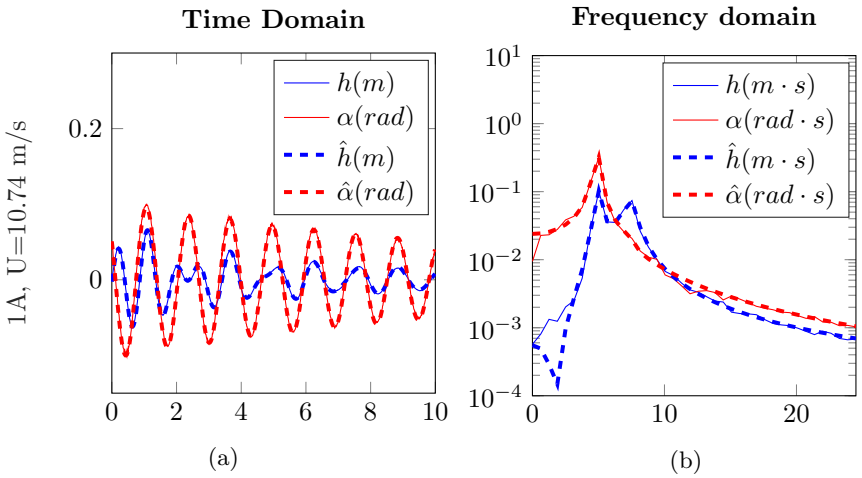

Figure 5: Measured response and simulations based on the best estimate of the model parameters at high wind speed for series 1A

The simulation based on the optimized CBHM and MULS estimates have joint coefficients of determination, $R_h^2 R_\alpha^2 = 0.932$ and $R_h^2 R_\alpha^2 = 0.996$ respectively for the 10 seconds time history shown to the left in Figure 4. It can be seen that the CBHM estimate ($R_h^2 R_\alpha^2 = 0.932$) is slightly off at the end of the 10 seconds time history while the MULS estimate ($R_h^2 R_\alpha^2 = 0.996$) is in agreement with the measured response in the right plot in Figure 4.

4.6.1. Shorter time histories

As shown in Figure 4, it is possible to fit a linearized system to the initial part of a post critical flutter time history. The aerodynamics of the section during flutter is not linear, however. This explains why the CBHM estimates had relatively lower $R_h^2 R_\alpha^2$ values because the correlation functions used were estimated from longer time histories (typically 60 seconds during flutter) which includes large pitching and heaving amplitudes giving rise to nonlinear aerodynamic effects.

Alternatively, if the correlation functions are estimated from the initial 10 seconds of recorded time history after the first vertical zero crossing, the accuracy of the CBHM estimate increases to $R_h^2 R_\alpha^2 > 0.95$ and on average $\mu(R_h^2 R_\alpha^2) = 0.972$ for all 5 tests. Because of the improved initial estimates, the accuracy of the MULS estimates increases to $\mu(R_h^2 R_\alpha^2) = 0.994$ for all 5 tests. This demonstrates three things:

1. The effect of nonlinear aerodynamics in the post critical flutter regime
2. The importance of choosing the proper time history length for the CBHM method
3. The importance of the accuracy of the initial estimate for the MULS method

The estimated damping ratios of the poles estimated at post critical flutter wind speeds are shown in Figure 10 at $U > 6$ m/s. It can be seen that there is a pole with positive damping and a pole with negative damping. The mode shape related to the poles are shown in Figure 7 where it can be seen that the excitation of the vertical degree of freedom, h, by the torsional dominated pole, ϕ_α, increases with the wind speed, U.

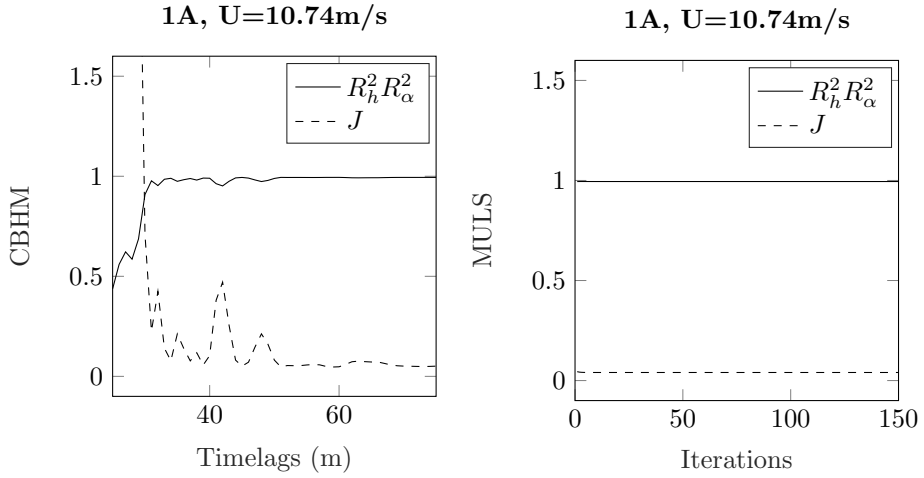

Figure 6: The $R_h^2 R_\alpha^2$ joint coefficient of determination and the residual sum of squares, J, for the CBHM method and the MULS method

5. Flutter Derivatives

Flutter derivatives estimated with the CBHM method and the MULS method having $R_h^2 R_\alpha^2 > 0.99$ are shown in Figure 8. Bin-averaging has been used to reduce the number of points in the plots. Each point represents the mean value of the estimated FD's from free vibration tests at approximately the same wind speed where $R_h^2 R_\alpha^2 > 0.99$ for all.

The negative H_1^* and H_4^* values indicate increasing aerodynamic damping and stiffness for the vertical dominated mode as a function of the reduced wind speed. The cross derivatives, H_2^* and H_3^* describe the aerodynamic coupling between the vertical DOF, h, and the torsional dominated mode. The cross derivatives, A_1^* and A_4^* describe the aerodynamic coupling between the torsional DOF, α, and the vertical dominated mode. It might be because of high damping of this mode, that the values of A_1^* and A_4^* are more scattered than the other derivatives in Figure 8. The positive A_3^* and H_3^* values indicate negative aerodynamic stiffness due to the excitation of the torsional dominated mode.

The flutter derivatives obtained after the onset of flutter for series 1G are shown in the right part of the shaded areas in Figure 8.

5.1. Torsional Flutter

Torsional flutter may occur if $A_2^* > 0$. In Figure 8 it is clearly seen that $A_2^* > 0$ at the low reduced wind speeds and $A_2^* < 0$ at higher reduced wind speeds. The A_2^* values for the $B/D = 10$ section obtained from forced motion tests in [20] have been transformed to the present notation and are shown as reference. The negative values obtained for series 1A indicate that torsional flutter can be avoided for the $B/D = 10$ section if the still air torsional damping is higher than the negative peak value for the aerodynamic torsional damping caused by the positive peak value for A_2^*.

5.2. Mode shapes

The mode shapes change as the wind speed increases. The magnitude of the complex vertical DOF normalized with the bridge deck width, h/B, and complex torsional DOF, α, in $\phi_{h/B}$ and ϕ_α are shown in Figure 7. It can be seen that the magnitude of the vertical DOF in the torsional dominated mode, $\phi_\alpha^{h/B}$ increases with the wind speed, U, which explains the values of the cross derivatives H_2^* and H_3^*. It can also be seen that the torsional DOF in the vertical dominated mode, $\phi_{h/B}^\alpha$, increases in series 1G while it is unaffected in series 1A. This might explain the slightly deviating values estimated for the cross derivatives A_1^* and A_4^* between the two series seen in Figure 8.

5.3. Static rotations

The aeroelastic and static forces on a bridge section model are subject to change with the mean angle of rotation [7, 8]. For configurations where $\omega_\alpha < \omega_h$, we suggest that the mass moment of inertia is raised instead of reducing the torsional stiffness to avoid static rotations. The mean angle of rotation, μ_α, during the free decay tests were zero at tunnel wind speeds, $U < 8.2$ m/s corresponding to $U/(B\omega_\alpha) < 6.8$. At the highest wind speeds, $U \approx 10.75$ m/s, the measured mean angle of rotation of the measured free response was $\mu_\alpha \approx 0.15^\circ$.

5.4. Amplitude effects

Several studies in the literature have shown that the torsional amplitude affects the derivatives [19, 23, 31] of bluff bodies. Flutter derivatives estimated from time histories starting when the torsional peaks has decreased to $\alpha \leq 3^\circ$ are shown in Figure 9 for the lower reduced wind speeds. At higher reduced wind speeds the joint coefficient of determinations decreases and the variance of the flutter derivatives increases. A noticeable change of sign is observed for A_2^* when the initial amplitude is reduced.

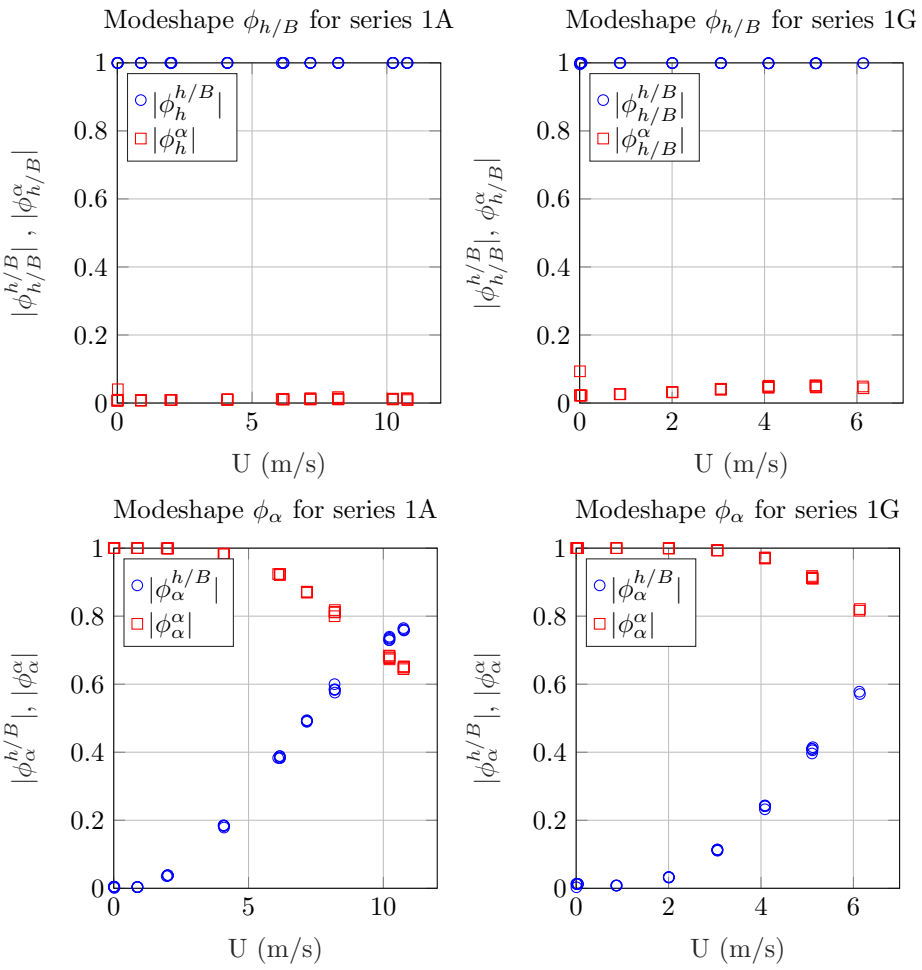

Figure 7: Magnitude of the complex vertical and torsional DOF in the two mode shapes estimated by the MULS method [3] for all wind speeds where $R_h^2 R_\alpha^2 > 0.99$.

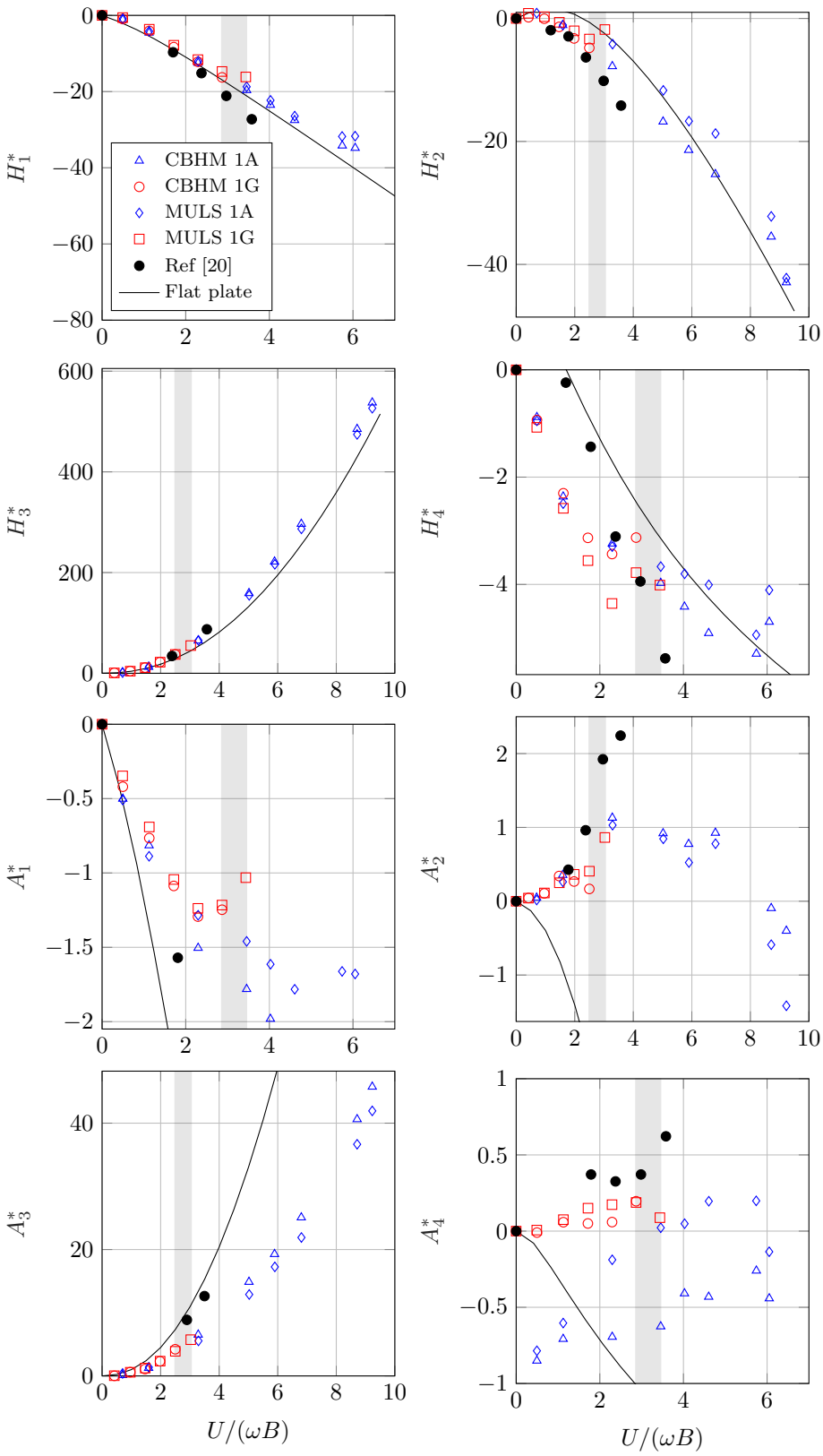

Figure 8: Bin-averaged flutter derivatives estimated by CBHM [14] and MULS [3]. The non-dimensional critical flutter wind speed, $U_{cr}/(\omega_{cr}B)$, for series 1G is located in the shaded areas. The legends in the upper left plot applies to all plots

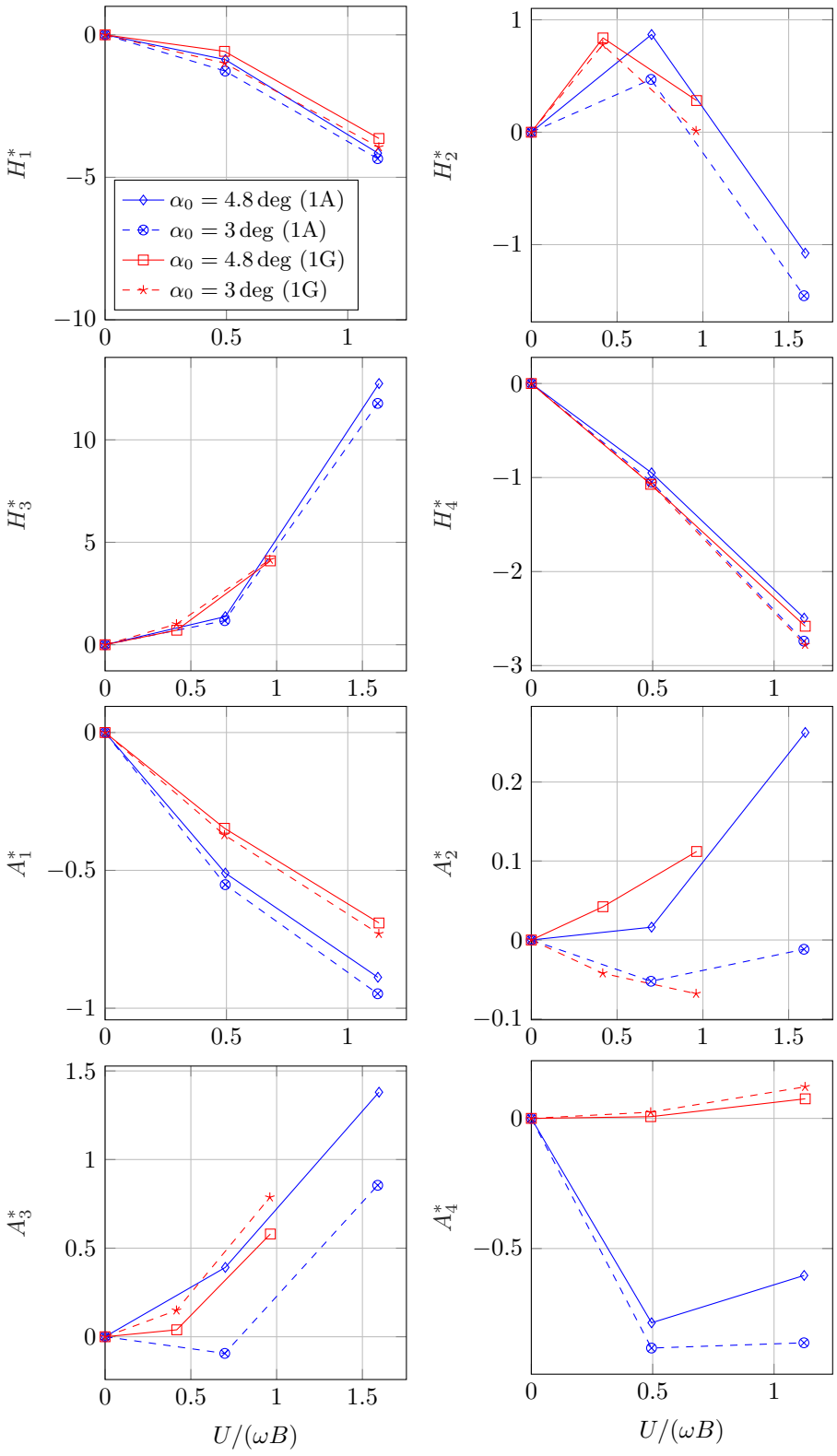

Figure 9: Bin-averaged flutter derivatives estimated by the MULS method [3] starting from initial amplitudes of $\alpha_0 = 4.8^\circ$ and $\alpha_0 = 3^\circ$ respectively

6. Flutter analysis

A third order polynomial was fitted to each of the flutter derivatives estimated by the MULS method in Figure 8. These polynomials were then used in a theoretical flutter analysis of the frequencies and damping ratios of the $B/D = 10$ sections under wind action shown in Figure 10. Furthermore, the mechanical still air damping and stiffness matrices given in Table 3 are used to calculate the modal parameters for increasing wind speeds by an iterative complex eigenvalue analysis described in [1]. The iterations are conducted mode-by-mode at each wind speed until the frequency of the mode has converged with the frequency used for K in the aerodynamic matrices given in Equation (2).

The thick dashed lines in Figure 10 show the modal parameters calculated using the same K for all coefficients in the aerodynamic matrices similar to Equation (2). The critical flutter wind speed is estimated to $U_{cr} = 4.89$ m/s which is lower than the highest wind speed observed where the system was stable, $U_1 = 5.10$ m/s. It is seen that the gradient of the damping curve is low which indicates soft and damping driven flutter. This agrees well with the positive A_2^* values in the range of reduced wind speeds where $2 \leq U/(\omega B) \leq 3$. Hence, the calculated critical flutter wind speed is very sensitive to the still air damping value and the curve fit to the experimentally estimated A_2^* values.

The thin solid lines in Figure 10 represent the modal parameters calculated using ω_h for H_1^*, H_4^*, A_1^*, H_4^* and ω_α for A_2^*, A_3^*, H_2^*, H_3^* used in Equation (7). The flutter wind speed calculated using this method in the iterations is $U_{cr} = 5.14$ m/s which is closer to the experimental flutter speed observed. The increased accuracy is caused by the fact that the implied approximation [5, 33] is used both in the identification of the flutter derivatives and in the iterative calculations of the modal parameters.

The scatter in Figure 10 shows the experimentally estimated values where the joint coefficient of determination, $R_h^2 R_\alpha^2 > 0.99$. It can be seen that the frequencies and damping ratios estimated in the post flutter regime fits well to the remaining data. The thin dot-dashed lines for series 1G show the modal parameters calculated using least square curve fits to the FD's given in [20]. The value of the critical flutter speed found in the present study is approximately 20% higher compared to the flutter speed calculated using the FD's given in [20]. Since the critical flutter wind speed is underestimated it is a conservative estimation of the flutter speed, but higher accuracy are obtained using the FD's estimated in the present tests.

For series 1A, flutter is not observed. Instead, it is seen that the damping decreases until $U \approx 5$ m/s, where it starts to increase again. This agrees well with the curvature of A_2^* shown in Figure 8. In order to avoid extrapolation, the modal parameters calculated based on the FD's in [20] are not conducted for $U/(\omega B) > 4$ ($U = 5$ m/s) in Figure 10.

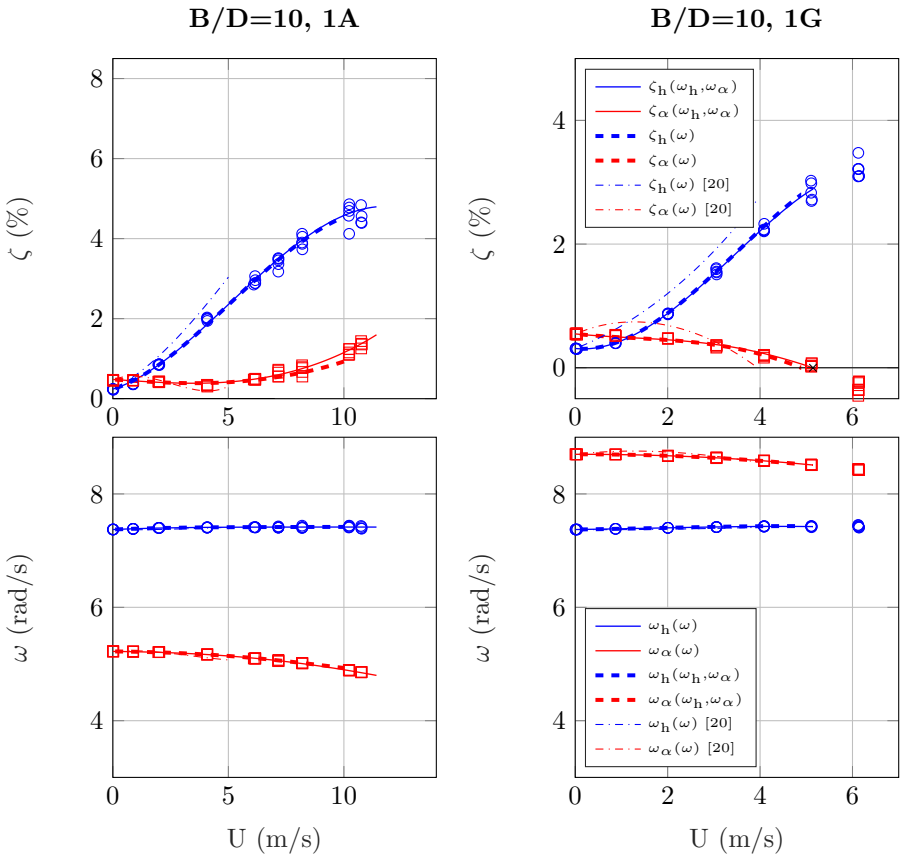

Figure 10: The estimated frequencies and damping ratios where $R_h^2 R_\alpha^2 > 0.99$ are shown with circular and square markers. The frequencies and damping ratios obtained by iterative mode-by-mode flutter analysis are shown as functions of the tunnel wind speed

7. Discussion

In Figure 8, the flutter derivatives were estimated by an iterative CBHM procedure to find the optimum number of discrete time lags. This was done by evaluating the accuracy of the estimated model parameters by the joint coefficient of determination, $R_h^2 R_\alpha^2$, introduced in Equation (11). Bin-averaging and rejection of estimated model parameters having a joint coefficient of determination value, $R_h^2 R_\alpha^2 < 0.99$ reduced the random errors. The flutter derivatives estimated by the MULS method generally agreed with the best CBHM estimates, but higher accuracy was achieved giving higher values for $R_h^2 R_\alpha^2$ as shown in Table 2. Nevertheless, the accuracy of the final estimate by the MULS method depends on the accuracy of the initial CBHM estimate that increases with the measurement time if the system is linear. In this case, the accuracy increases using longer time series even though the MULS estimate is only based on e.g.

the first 10 seconds. For non-linear system response, e.g. flutter, it is crucial to use short time histories from the initial part only as shown in Section 4.6.

Deviating values for A_4^* were observed, which might be explained by the obstacles involved in observing very small changes in the frequency of a mode with large damping. The values estimated were close to zero. Since they are almost zero, their effect on the stiffness matrix of the section model in wind is small. Even though they are larger than zero, it may not be important for the development of the unstable flutter mode according to e.g. the sensitivity study conducted in [24]. The derivatives associated with the torsional dominated mode, A_3^*,A_2^*,H_3^*,H_2^* were well identified because this mode has lower damping and is therefore more observable compared to the vertical dominated mode. The effective aerodynamic stiffness and damping matrices as well as the flutter derivatives were uniquely identified because both modes were excited in the beginning of each time series.

7.1. On torsional flutter

The estimated A_2^* values seem to peak at $U/(\omega B) \approx 5$ whereafter they decline as shown in Figure 8. Since the A_2^* values are small and eventually negative, torsional and coupled flutter were avoided in series 1A. This was caused by an increase in the still air damping due to the large mass moment of inertia making $\gamma_\omega < 1$. Nevertheless, flutter may occur even for very low positive A_2^* values which was seen in Figure 10 for series 1G which had a lower still air damping value. Future tests might answer why negative aerodynamic damping is changed to positive aerodynamic damping at higher reduced wind speeds.

The complex mode shapes shown in Figure 7 illustrate that the motion in the post flutter regime is not only torsional but the vertical degree of freedom is excited by the unstable mode as well. Therefore it seems imprecise to characterize it as 'SDOF *torsional* flutter'. The complex eigenvalues identified in the post flutter regime showed that there was one mode with negative damping and one mode with positive damping. The observed flutter motion can be seen in the measured time series shown in Figure 4.

The differences in flutter derivatives for the $B/D = 10$ section given in [20] compared to [21] and the present results should be carefully considered. In [20] the A_2^* values are all positive, but the curve seems to level off at the highest wind speed reached. Some of the tests discussed in [21] showed negative A_2^* values for smaller pitching motion amplitudes and positive values for the largest amplitudes. The pitching motion amplitudes during the present free vibration tests were up to three times larger than the largest amplitudes discussed in [21]. However, amplitude effects were observed. Using an initial amplitude of $\alpha = 3^\circ$ instead of $\alpha = 4.8^\circ$ caused negative values for A_2^* at reduced wind speeds $U/(\omega B) < 1.5$. This agrees well with the amplitude dependencies described in [23].

The negative A_2^* values shown in Figure 9for lower pitching motion amplitudes might be explained by a smaller separation bubble at the leading edge of the section and a longer zone with reattached flow.

7.2. Amplitude effects

The flutter derivatives is based on a linearization of the aeroelastic forces and was originally intended only to be valid for small pitching motion amplitudes [28, 30]. The good agreement between simulations of linear systems and the measured response in the present study indicate that the aeroelastic forces can be linearized at higher amplitudes, but the estimated flutter derivatives are only valid under similar conditions under which they were obtained and may change according to the pitching and heaving motion amplitudes as shown for A_2^* in Figure 9.

The $R_h^2 R_\alpha^2$ values were based on 10 seconds time histories. Longer time histories would cause larger discrepancies and lower $R_h^2 R_\alpha^2$ values due to the amplitude motion effects. This was shown for the CBHM estimates at post critical flutter wind speeds in Section 4.6.

It was not possible to estimate the flutter derivatives at reduced wind speeds higher than $U/(\omega B) \approx 1.5$ for the lower pitching motion amplitudes because the free decaying response vanished into pure buffeting due to the aerodynamic damping.

7.3. Static rotations

The static angle of rotation increased to approximately 0.15° in the present study at the highest wind speed, which seems small compared to the studies conducted in [19, 23], but may have a small affect. Different end effects, surface roughness and sharpness of the edges of the section models may affect the flow around the section and the wake which can affect the FD's.

7.4. Flutter wind speed

The flutter derivatives estimated for the present $B/D = 10$ section are compared with [20] in Figure 8. There is a reasonable agreement for the general tendencies of the derivatives. For A_2^*, however, there is an inflection point which coincides with the highest reduced wind speed in [20]. Furthermore, the A_2^* values in [20] are larger than in the present study. This could possibly explain why the observed flutter wind speed in the wind tunnel is approximately 20% higher in the present study compared to the flutter speed calculated using the FD's given in [20]. If the flutter wind speed is calculated by the FD's estimated in the present study, a better agreement with the experimentally observed flutter wind speed is achieved, which seems to indicate that the results in the present study are correct, however.

8. Conclusions

The flutter derivatives of a sharp-edged $B/D = 10$ rectangular section was estimated by an optimized system identification method based on an iterative CBHM [4, 13, 14] procedure in combination with the MULS [3] method. The flutter derivatives were obtained from coupled free vibration tests at very high reduced wind speed and even after the onset of flutter. The accuracy of the

estimated derivatives was evaluated by a simple method relying on the R^2 coefficients of determination between the measured and simulated vertical and torsional signals. The product of the R^2 coefficients for the vertical and torsional signals were denoted the joint coefficient of determination, $R_h^2 R_\alpha^2$.

The CBHM estimate having the highest $R_h^2 R_\alpha^2$ value was used as the initial estimate for the MULS method. An improvement of the accuracy of the initial estimate improved the accuracy of the final MULS estimate. This may indicate that local minima are present and that different minimization algorithms might lead to different results. By the present optimization of the methods, it was possible to estimate the FD's by free vibration tests in both the pre- and post critical flutter regime with a joint coefficient of determination $R_h^2 R_\alpha > 0.99$ for 10 seconds of time data starting at the first vertical zero crossing after the release of the section.

Due to the stable behavior of the section model when $\omega_\alpha < \omega_h$, the flutter derivatives were estimated at reduced wind speeds $U/(\omega B) \approx 9$ which is unusually high for free vibration tests. An inflection point for the positive A_2^* values prevented the onset of torsional flutter. This implies that torsional flutter can be avoided for the $B/D = 10$ if the structural still air damping balances the negative torsional aerodynamic damping expressed by the positive peak value for A_2^* at the inflection point.

The influence of pitching motion amplitude on A_2^* for $U/(\omega B < 1.5)$ showed negative values for smaller amplitudes and positive values for the largest amplitudes. A change in the gradient of the estimated A_2^* values for small amplitudes indicates that they may change sign to positive at $U/(\omega B) > 1.5$. It is unlikely, however, that positive A_2^* values larger than the peak value, $A_2^* = 0.86$ at $U/(\omega B) = 3.03$ occur because torsional flutter remained unobserved at the highest reached tunnel wind speed for test series 1A corresponding to $U/(\omega B) \approx 10$.

Acknowledgement

The tests were conducted in collaboration with Michele Øvre. Michael Lenius and Jesper R. Læsø implemented the MULS method in their master thesis which we gratefully acknowledge. Special thanks to Svend Ole Hansen Aps and the involved employees for their continuous support and help during the preparation and execution of the experiments. The anonymous reviewers are gratefully acknowledged for their comments and suggestions.

References

[1] T.J.A. Agar. Aerodynamic flutter analysis of suspension bridges by a modal technique. *Engineering Structures*, 11(2):75 – 82, 1989.

[2] M.S. Andersen, J. Johansson, A. Brandt, and S.O. Hansen. Aerodynamic stability of long span suspension bridges with low torsional natural frequencies. *Engineering Structures*, 120:82 – 91, 2016.

[3] G. Bartoli, S. Contri, C. Mannini, and M. Righi. Toward an improvement in the identification of bridge deck flutter derivatives. *Journal of Engineering Mechanics*, 135(8):771–785, 2009.

[4] J.M.W. Brownjohn and J.B. Jakobsen. Strategies for aeroelastic parameter identification from bridge deck free vibration data. *Journal of Wind Engineering and Industrial Aerodynamics*, 89(13):1113 – 1136, 2001.

[5] Xinzhong Chen and Ahsan Kareem. Efficacy of the implied approximation in the identification of flutter derivatives. *J. Struct. Eng*, 130(12):2070–2074, 2004.

[6] Stefano de Miranda, Luca Patruno, Francesco Ubertini, and Giuseppe Vairo. On the identification of flutter derivatives of bridge decks via {RANS} turbulence models: Benchmarking on rectangular prisms. *Engineering Structures*, 76:359 – 370, 2014.

[7] G. Diana, G. Fiammenghi, Belloli. M., and D. Rocchi. Wind tunnel tests and numerical approach for long span bridges: The messina bridge. *Journal of Wind Engineering and Industrial Aerodynamics*, 122:38 – 49, 2013. The Seventh International Colloquium on Bluff Body Aerodynamics and Applications (BBAA7).

[8] G. Diana, D. Rocchi, T. Argentini, and S. Muggiasca. Aerodynamic instability of a bridge deck section model: Linear and nonlinear approach to force modeling. *Journal of Wind Engineering and Industrial Aerodynamics*, 98(6):363 – 374, 2010. 6th International Colloquium on Bluff Body Aerodynamics and Applications.

[9] M. Gu and X. Qin. Direct identification of flutter derivatives and aerodynamic admittances of bridge decks. *Engineering Structures*, 26(14):2161 – 2172, 2004.

[10] M. Gu, R. Zhang, and H. Xiang. Identification of flutter derivatives of bridge decks. *Journal of Wind Engineering and Industrial Aerodynamics*, 84(2):151 – 162, 2000.

[11] M. Gu, R. Zhang, and H. Xiang. Parametric study on flutter derivatives of bridge decks. *Engineering Structures*, 23(12):1607 – 1613, 2001.

[12] S.R. Ibrahim and E.C. Mikulcik. The experimental determination of vibration parameters from time responses. *The Shock and Vibration Bulletin*, 46(5):187–196, 1976.

[13] Jasna Bogunović Jakobsen. *Fluctuating wind load response of line-like engineering structure with emphasis on motion-induced wind forces*. PhD thesis, Department of Structural Engineering, University of Trondheim, Norway, 1993.

[14] J.B. Jakobsen and E. Hjorth-Hansen. Determination of the aerodynamic derivatives by a system identification method. *Journal of Wind Engineering and Industrial Aerodynamics*, 57(2):295 – 305, 1995.

[15] J. Johansson, M.S. Andersen, and M.S. Øvre. Non-flutter design principle for long span bridges. In *Proceedings of the Eighth Asia-Pacific Conference on Wind Engineering*, 2013.

[16] J-N Juang and Richard S Pappa. An eigensystem realization algorithm for modal parameter identification and model reduction. *Journal of guidance, control, and dynamics*, 8(5):620–627, 1985.

[17] Y. Li, H. Liao, and S. Qiang. Weighting ensemble least-square method for flutter derivatives of bridge decks. *Journal of Wind Engineering and Industrial Aerodynamics*, 91(6):713 – 721, 2003.

[18] L. Luca Caracoglia, Partha P. Sarkar, Frederick L. Haan Jr, Hiroshi Sato, and Jun Murakoshi. Comparative and sensitivity study of flutter derivatives of selected bridge deck sections, part 2: Implications on the aerodynamic stability of long-span bridges. *Engineering Structures*, 31(9):2194 – 2202, 2009.

[19] Claudio Mannini, Gabriele Sbragi, and Gnter Schewe. Analysis of self-excited forces for a box-girder bridge deck through unsteady {RANS} simulations. *Journal of Fluids and Structures*, 63:57 – 76, 2016.

[20] M. Matsumoto, K. Mizuno, K. Okubo, and Y. Ito. Torsional flutter and branch characteristics for 2-d rectangular cylinders. *Journal of Fluids and Structures*, 21(57):597 – 608, 2005.

[21] M. Matsumoto, N. Shiraishi, H. Shirato, K. Shigetaka, and Y. Niihara. Aerodynamic derivatives of coupled/hybrid flutter of fundamental structural sections. *Journal of Wind Engineering and Industrial Aerodynamics*, 49(1):575 – 584, 1993.

[22] Masaru Matsumoto. Aerodynamic damping of prisms. *Journal of Wind Engineering and Industrial Aerodynamics*, 59(2):159 – 175, 1996.

[23] M. Noda, H. Utsunomiya, F. Nagao, M. Kanda, and N. Shiraishi. Effects of oscillation amplitude on aerodynamic derivatives. *Journal of Wind Engineering and Industrial Aerodynamics*, 91(1):101 – 111, 2003. Fifth Asia-Pacific Conference on Wind Engineering.

[24] O. Øiseth, A. Rönnquist, and R. Sigbjörnsson. Simplified prediction of wind-induced response and stability limit of slender long-span suspension bridges, based on modified quasi-steady theory: A case study. *Journal of Wind Engineering and Industrial Aerodynamics*, 98(12):730 – 741, 2010.

[25] N.K. Poulsen, A. Damsgaard, and T.A. Reinhold. Determination of flutter derivatives for the great belt bridge. *Journal of Wind Engineering and Industrial Aerodynamics*, 41(1):153 – 164, 1992.

[26] P.P. Sarkar, L. Caracoglia, F.L. Haan Jr., H. Sato, and J. Murakoshi. Comparative and sensitivity study of flutter derivatives of selected bridge deck sections, part 1: Analysis of inter-laboratory experimental data. *Engineering Structures*, 31(1):158 – 169, 2009.

[27] P.P. Sarkar, N.P. Jones, and R.H. Scanlan. System identification for estimation of flutter derivatives. *Journal of Wind Engineering and Industrial Aerodynamics*, 42(1):1243 – 1254, 1992.

[28] R.H. Scanlan and J.J. Tomko. Airfoil and bridge deck flutter derivatives. *Journal of the engineering mechanics division*, pages 1717–1737, 1971.

[29] Robert H. Scanlan. Amplitude and turbulence effects on bridge flutter derivatives. *Journal of Structural Engineering*, 123(2):232–236, 1997.

[30] T. Theodorsen. General theory of aerodynamic instability and the mechanism of flutter. *NACA Report*, 496:291–311, 1934.

[31] Fuyou Xu, Xuyong Ying, and Zhe Zhang. Effects of exponentially modified sinusoidal oscillation and amplitude on bridge deck flutter derivatives. *Journal of Bridge Engineering*, 21(5):06016001, 2016.

[32] Fuyou Xu and Zhanbiao Zhang. Free vibration numerical simulation technique for extracting flutter derivatives of bridge decks. *Journal of Wind Engineering and Industrial Aerodynamics*, 170(Supplement C):226 – 237, 2017.

[33] Fuyou Xu, Ledong Zhu, Xiaomeng Ge, and Zhe Zhang. Some new insights into the identification of bridge deck flutter derivatives. *Engineering Structures*, 75:418 – 428, 2014.

[34] F.Y. Xu, X.Z. Chen, C.S. Cai, and A.R. Chen. Determination of 18 flutter derivatives of bridge decks by an improved stochastic search algorithm. *Journal of Bridge Engineering*, 17(4):576–588, 2011.